

A SURVEY OF 3.3 μ M PAH EMISSION IN PLANETARY NEBULAE

ERIN C. D. SMITH¹, IAN S. MCLEAN²

(Received 2007 October 8)

Accepted to ApJ

ABSTRACT

Results are presented from a pilot survey of 3.3 μ m PAH emission from planetary nebulae using FLITECAM, an instrument intended for airborne astronomy with SOFIA. The observations were made during ground-based commissioning of FLITECAM's spectroscopic mode at the 3-m Shane telescope at Lick Observatory. Direct-ruled KRS-5 grisms were used to give a resolving power (R) \sim 1,700. Targets were selected from IRAS, KAO and ISO sources with previously observed PAH emission at longer wavelengths. AGB stars and PN with C/O ratios < 1 were also added to the target list in order to test PAH detection thresholds. In all, 20 objects were observed. PAH emission was detected in 11 out of 20 observed targets.

Subject headings: infrared: general — techniques: spectroscopic — planetary nebulae: general — stars: AGB and post-AGB — astrochemistry: PAHs

1. INTRODUCTION

The broad infrared emission features observed at 3.3, 6.2, 7.7, 8.6, and 11.2 μ m have been the subject of astronomical investigation since their first observation in the 1970s (Gillett et al. 1973; Gillett et al. 1975). Through comparison to laboratory spectra and additional observational data these bands have been attributed to bending and stretching modes of polycyclic aromatic hydrocarbons (PAHs) (Sellgren 1984; Léger & Puget 1984; Geballe et al. 1985). PAHs are formed by aromatic structures of carbon and hydrogen which can bind together into larger assemblies, forming a family of small molecules such as pyrene, coronene and others. Emission features associated with PAHs have been observed in a wide variety of objects, including planetary nebulae, HII regions, proto-stellar clouds and star-forming galaxies (Peeters et al. 2002; Hony 2002). This ubiquity shows PAHs to be potentially important components of the ISM, and has led to several studies aimed at correlating PAH emission with region characteristics (Tokunaga et al. 1991; Roche et al. 1996; Cohen & Barlow 2005; Peeters et al. 2002; van Diedenhoven et al. 2004). Recent surveys (Peeters et al. 2002, van Diedenhoven et al. 2004) using space-based telescopes have shown variability in the PAH emission. Peeters et al. (2002) introduced a classification scheme which grouped 6.2, 7.7 and 8.6 μ m PAH spectra into three groups based on band FWHM, peak wavelength and overall shape. HII regions, reflection nebulae, and young stellar objects tended to exhibit Class A_{6–9} PAH behavior, while evolved stellar objects like planetary nebulae and post-AGB stars exhibited class B_{6–9} emission. A small number of objects, tending to be very young AGB stars, exhibited class C_{6–9} PAH emission (Sloan et al. 2007). Van Diedenhoven et al. (2004) expanded this classification to the 3.3 μ m and 11.2 μ m bands. Variations in the 3.3 micron feature were found to be smaller than those in the 7.7 and 6.2 micron

features. This is explained by the fact that the 3.3 and 11.2 μ m features are due to stretching and out-of-plane bending modes of the C-H bonds in the PAH molecules, while the 6.2 and 7.7 μ m features arise from stretching in the C-C bonds (Allamandola et al. 1989). Tokunaga et al. (1991) and van Diedenhoven et al. (2004) classified the 3.3 micron feature into two classes: class A_{3.3}, or class 1, with emission centered at 3.290 μ m and a FWHM of 0.040 μ m, and class B_{3.3}, or class 2, which have a FWHM of 0.037 μ m with emission centered at 3.293 μ m (class B_{1.3.3}) or 3.297 μ m (class B_{2.3.3}). Planetary nebulae and their evolutionary precursors tended to be class A_{3.3} objects. While other emission features are sensitive to PAH charge state, comparisons with laboratory data show the 3.3 μ m feature to arise from neutral PAHs, rather than PAH cations (Allamandola et al. 1989).

PAHs are produced in the hot outflows accompanying the last stages of evolution of low and intermediate-mass stars. As a star evolves off the Asymptotic Giant Branch (AGB), a period of dramatic mass loss begins. Roche et al. (1996) found a threshold C/O ratio for 3.3 μ m PAH emission in planetary nebulae of ~ 0.6 . A study of 7 and 8 μ m emission by Cohen & Barlow (2005) found a roughly consistent threshold ratio of 0.56 ± 0.3 . In nebulae with lower C/O ratios, nebular carbon is expected to be incorporated in silicates and CO, while carbon-rich nebulae produce hydrocarbons including PAHs (Allamandola et al. 1989). PAH emission is caused by UV excitation. In planetary nebulae the stellar remnant bathes the expanding gas shell with UV photons which produce elemental nebular lines and also excite the vibrational and stretching modes of PAH molecules. The relaxation of these modes produces the broad infrared emission features which have been observed in several planetary nebulae, as well as their evolutionary precursors: proto-planetary nebulae and post-AGB stars (Matsuura et al. 2005; Justtanont et al. 1996).

This survey has three purposes: investigate the properties of 3.3 μ m PAH emission in planetary nebulae by expanding the analysis performed by Roche et al. (1996) and Cohen & Barlow (2005); expand the classification of 3.3 micron emission to a larger sample of planetary neb-

¹ Department of Physics and Astronomy, UCLA, Los Angeles, CA 90095-1562; erincds@astro.ucla.edu

² Department of Physics and Astronomy, UCLA, Los Angeles, CA 90095-1562; mclean@astro.ucla.edu

ulae using a higher resolution than previous surveys; and demonstrate the FLITECAM instrument's spectroscopy mode in a survey likely to be undertaken once aboard SOFIA.

As part of the science verification of the FLITECAM instrument for SOFIA, we proposed spectroscopic and narrow band imaging observations of the $3.3\ \mu\text{m}$ PAH feature, together with atomic and molecular emission, in post-AGB stars, planetary nebulae, HII regions and reflection nebulae. With the significantly increased sensitivity of stratospheric observations, the overall goal of this project is to trace the origin and evolution of PAHs from their birth environment through their processing in the ISM to their incorporation in proto-stellar material. The $3.3\ \mu\text{m}$ feature is quite broad and typically resolved at $R\sim 300$. FLITECAM's grism mode has a higher spectral resolution that allows investigation of not only the PAH feature itself, but also PAH interaction with ionized and neutral gas. In principle, higher resolution allows subtle changes in PAH emission shape to be observed. In addition, FLITECAM's narrow-band imaging capability allows one to study the spatial distribution of PAH emission in spatially-resolved objects. FLITECAM offers three advantages for this study: a wide field of view (~ 8 arc minutes diameter) for imaging studies, good spectral resolution ($R\sim 1700$) and, when used with SOFIA, a reduced water vapor overburden and colder telescope thus significantly reducing the background at this wavelength.

Prior to the start of SOFIA flight operations we decided to try a pilot-study from a ground-based observatory in order to develop the methodology for this project. Although the low water-vapor advantage is completely lost and backgrounds are much increased for a ground-based telescope, we have successfully detected the $3.3\ \mu\text{m}$ PAH feature, with relatively high spectral resolution, in several planetary and proto-planetary nebulae. Wherever possible, the strength of the emission has been quantified and compared with other physical properties such as C/O ratio. The pilot study demonstrates the potential for more sensitive PAH studies when SOFIA is operational. Our results and methods, including a brief description of the instrument, are described in this paper.

Target selection, the FLITECAM grism mode and the observations are described in §2, data reduction methods are explained in §3 and results are presented in §4. Analysis and conclusions are given in §5.

2. OBSERVATIONS

2.1. Target Selection

Targets for our $3.3\ \mu\text{m}$ survey were selected from ISO, KAO and IRAS observations of planetary nebulae, proto-planetary nebulae and post-AGB stars. Our sample was compiled based on the reported presence of PAH emission in longer wavelength bands observed from space, as well as practical issues of signal-to-noise limitations at a low-altitude ground-based site. Of the 20 objects in the survey, 13 had previous long-wave PAH detection in at least one band (Cohen et al. 1989; Jourdain de Muizon et al. 1990; Rinehart et al. 2002). Additional sources were added in order to extend the sample to post-AGB stars and proto-planetary nebulae. Since PAH emission is expected only in objects with a carbon-rich dust chemistry, all but 3 objects have C/O ratios above the threshold ra-

tio for PAH emission determined by Roche et al. and Cohen & Barlow. One O-rich nebula shows a somewhat mixed dust chemistry, while the remaining two O-rich objects were used as a test of methodology (Jourdain de Muizon et al. 1990). The targets in this sample represent a somewhat larger range in morphology, size and brightness than would normally be selected for a survey of this type. This was done in order to meet the broad goals of the pilot study and to facilitate the fullest possible science verification of the FLITECAM grism mode.

All data presented here were obtained using the Shane 3-meter telescope at Lick Observatory, Mt. Hamilton, CA, with the FLITECAM instrument attached. Observations were collected over the course of five separate observing runs from May 2004 to October 2006. Table 1 lists all the targets, total observation times, and the standard stars used to remove telluric absorption lines. Shorthand names (such as BD30 for BD+30°3639) are used throughout the text for simplicity, but full names are given in Table 1.

2.2. Instrumentation

As mentioned above, our pilot-study of $3.3\ \mu\text{m}$ emission from PN was carried out as part of the commissioning and performance verification of a new instrument called FLITECAM (First Light Test Experiment Camera). FLITECAM is a $1\text{--}5\ \mu\text{m}$ camera developed by us at the UCLA Infrared Laboratory (P.I.: McLean) for NASA's SOFIA (Stratospheric Observatory for Infrared Astronomy) project. SOFIA is a modified Boeing 747-SP airplane with a 2.5-meter f/19.6 bent-Cassegrain telescope operating at altitudes up to 45,000 ft and therefore above 99% of the atmosphere's water vapor content. Most of the SOFIA instruments are designed for much longer wavelengths, but because FLITECAM operates in the near-infrared, and because the f/17 optics of the Lick 3-meter telescope provides a plate scale similar to that of SOFIA, FLITECAM can be used from the ground without additional optics. Performance and technical details of the instrument are described in McLean et al. 2006. First light was obtained in October 2002 at Lick Observatory and the instrument has accumulated data with the 3-meter telescope on eight separate occasions. Photometric results from a narrow band survey of nearby star-forming regions for methane-bearing planetary mass objects have been published elsewhere (Mainzer and McLean 2003; Mainzer et al. 2004; McLean et al. 2006).

Briefly, FLITECAM utilizes large refractive optics to inscribe an ~ 8 arc minute diameter FOV on a 1024×1024 InSb ALADDIN III detector with a plate scale of just under 0.5 arc seconds per pixel. The instrument is cooled with 20 liters of LN_2 and 20 liters of LHe and can be operated in either the up-looking position (Lick) or the horizontal position (SOFIA). Another feature is a dual filter wheel which houses standard broadband filters, several narrow band filters plus a suite of three direct-ruled KRS-5 grisms and their appropriate order-sorting filters. Each grism can be used in one of three orders giving a total of 9 settings to cover the entire $1\text{--}5\ \mu\text{m}$ region. The KRS-5 grisms provide a moderate resolution spectroscopy mode in conjunction with fixed slits of either $1''$ or $2''$ width and $60''$ total length to yield resolving powers of $R\sim 1700$ and 900 respectively (Smith and McLean 2006). When

TABLE 1
TARGET LIST AND OBSERVING LOG

Object	R.A. (J2000.0)	Dec. (J2000.0)	Object Type	PAH Detected? ^(a)	UT Date of Observation
M 3–35	20 21 03.769	+32 29 23.86	PN	Y	July 25 2005
NGC 7027	21 07 01.593	+42 14 10.18	PN	Y	Oct 23 2005
HB 5	17 47 56.187	−29 59 41.91	PN	Y	May 9 2006
IC 5117	21 32 31.027	+44 35 48.53	PN	Y	July 22 2005
BD+30°3639	19 34 45.2323	+30 30 58.936	PN	Y	May 6 2004
M 2–43	18 26 40.048	−02 42 57.63	PN	Y	July 25 2005
IRAS21282+5050 ^(b)	21 29 58.42	+51 03 59.8	PN	Y	July 23 2005
Hen 2–459	20 13 57.898	+29 33 55.94	PN	Y	July 23 2005
WHME–1	19 14 59.755	+17 22 46.01	PN	?	July 22 2005
J900 ^(c)	06 25 57.275	+17 47 27.19	PN	?	Oct 8 2006
NGC 6886	20 12 42.813	+19 59 22.65	PN	Y	Oct 8 2006
NGC 6790	19 22 56.965	+01 30 46.45	PN	Y	May 7 2006
M 4–18	04 25 50.831	+60 07 12.72	PN	Y	Oct 22 2005
AFGL 3068	23 19 12.39	+17 11 35.4	Mira	Cont	Oct 20 2005
AFGL 3116	23 34 27.66	+43 33 02.4	C*	Cont	Oct 21 2005
AFGL 337	02 29 15.3	−26 05 55.67	Mira	Cont	Oct 22 2005
YY Tri	02 18 06.6	+28 36 48.3	C*	Cont	Oct 07 2006
M 2–9	17 05 37.952	−10 08 34.58	PN (O-rich)	N	June 4 2004
NGC 3242	10 24 46.107	−18 38 32.64	PN (O-rich)	N	May 9 2006
NGC 6210	16 44 29.491	+23 47 59.68	PN (O-rich)	N	May 7 2006

^a Cont: Continuum Object; C*: Carbon-rich AGB star; o-rich: oxygen-rich chemistry; ?: possible PAH detection Y: PAH detected, N: No PAH detection

^b IRAS21282+5050 is also named PN G093.9–00.1

^c J900 is also PN G 194.2+02.5

airborne, FLITECAM will be the only instrument providing spectral coverage from 2.5–5.5 μ m with a low water vapor and low background environment.

2.3. Observations

FLITECAM’s imaging mode was used to place each object on the selected slit, and the observatory’s offset CCD guide camera was used to hold the source on the slit. Spectroscopic observations were made in a standard ABBA nod pattern. Typically, integrations of 300 s each (3 s exposure with 100 coadds) were taken with the object placed at two positions, designated A and B, separated by $\sim 26''$ on the $\sim 60''$ long entrance slit of FLITECAM. Shorter exposure times were used for brighter objects. The total number of ABBA cycles depends on the object, but all targets were observed for a minimum of one cycle. Total integration times per object ranged from 20 minutes to 1.5 hours. Signal-to-noise ratios were typically greater than 10 (10%) per resolution element. Seeing conditions were $\sim 1''.0 - 1''.2$ and a slit width of $1''.0$ (~ 2 pixels) was used for all observations, except in the case of HB 5 for which we used a $2''.0$ (4 pixels) slit because of poorer seeing.

The grism mode selected provides coverage from 3.0–3.4 μ m. This spectral region exhibits significant contamination from absorption lines of terrestrial water vapor, making ground-based observations very difficult. In principle, these absorption features can be removed by observations of standard stars. Two methods were used to obtain satisfactory telluric corrections; 1) ATRAN models of the atmosphere (Lord 1979); 2) observations of a bright A0V star or MIII giant star at an airmass very close to that of the target object. Great care was taken to ensure the telluric standard did not saturate the FLITECAM detector. Arc lamp spectra, taken at the end of the night, and OH night-sky lines in the observed spectra, were used for wavelength and dispersion calibration.

A white-light spectrum and a corresponding dark frame were also obtained for flat-fielding. Calibration stars are listed in Table 1.

3. DATA REDUCTION METHODS

3.1. Redspec

Survey data were reduced using REDSPEC, an IDL-based software package developed at UCLA for spectra obtained with the Keck NIRSPEC instrument by S. Kim, L. Prato and I. McLean³. REDSPEC was modified for use on FLITECAM data by adding routines to flip the raw spectra, to automatically subtract nod pairs to enable spatial rectification of thermal-IR spectra (in which the traces are hard to see against the background), and to apply FLITECAM wavelength solutions to the spectra.

To extract spectra free from atmospheric background and uneven detector response, the difference of an A/B image pair was formed and flat-fielded. The flat-fielded difference frame was then rectified using the spatial and spectral maps and the raw spectrum produced by summing 5–10 rows from each trace in the rectified image. The extracted traces (one positive, one negative) are then subtracted again to produce a positive spectrum with residual night-sky emission line features removed, unless a line was saturated. Telluric standard star spectra were reduced in the same way. After interpolating over the intrinsic hydrogen absorption lines, the reduced target spectrum was divided by the reduced calibrator star spectrum to remove telluric features. The true slope of the target spectrum was restored by multiplication with a blackbody spectrum of $T_{eff} = 9500$ K for an A0 V star, and $T_{eff} = 3000$ K for an MIII star (Tokunaga 1991). Finally, the spectra reduced from multiple A/B pairs were averaged together to improve the signal-to-noise ratio.

³ See <http://www2.keck.hawaii.edu/inst/nirspec/redspec/index.html>

3.2. ATRAN telluric correction

Ground-based thermal infrared observations are dramatically affected by variability in atmospheric water vapor and background emission. Therefore, good telluric correction is critical to accurate reduction of thermal IR spectra. In many cases, appropriate telluric standards are either too faint for good correction, or too widely separated for a good airmass match. In addition, the infrared backgrounds at Lick observatory can change during observations of target objects, making accurate telluric correction using observed standards very difficult. As an alternative to observed telluric standards, ATRAN, an atmospheric modelling program developed by Steve Lord, was used to generate artificial telluric calibrator spectra at the target's zenith angle and airmass. ATRAN models allow tweaking of water vapor over-pressure and other atmospheric conditions to produce optimized telluric corrections for each target. Spectra of targets with high S/N ratios (NGC 7027, BD+30°3639) showed no appreciable differences between telluric-corrected spectra using observed standard stars and ATRAN-corrected spectra. Low S/N object spectra were noticeably improved using ATRAN-produced telluric standards. This makes sense because low S/N targets were observed for longer total time periods than high S/N targets, increasing the contribution of atmospheric variability in the resulting spectrum. While optimized ATRAN models can be fit individually to each target AB pair in a long sequence, the single observed telluric calibrator is only a good fit for one moment in time.

ATRAN models were computed using a standard 2 layer atmosphere at 4000 ft elevation using the appropriate zenith angle for each target observation. The water vapor over-pressure was varied from 8 to 12 mm (around the standard predicted value of 10 mm) for each target object to obtain the best fit to the data. This produced a normalized, flat-fielded calibrator spectrum. Each target observation was reduced using the REDSPEC software package as described in §3.1, but without division by a calibrator. Instead, the reduced target spectrum was divided by the ATRAN-produced telluric calibrator spectrum.

4. RESULTS

4.1. Overview

Those objects that yielded the best PAH spectra tended to be young, high-excitation compact planetary nebulae. Objects such as NGC 3242 for example, were too low in surface brightness to yield a useful spectrum given the high background of the ground-based observations. Very bright objects, such as AFGL 3086, also did not yield a PAH detection because the central object saturated the FLITECAM detector, even at the shortest possible exposure times, and any extended PAH emission located far enough away from the central object so as to avoid saturation was too low in surface brightness to be detected. All reduced spectra show residual structure from atmospheric water vapor lines that could not be removed. L-band observations are difficult at Lick Observatory because the site is only 4209 ft above sea level, and is located in a particularly humid area. These conditions lead to highly variable telluric features, often variable on the timescale of one nod (5 minutes). While the telluric

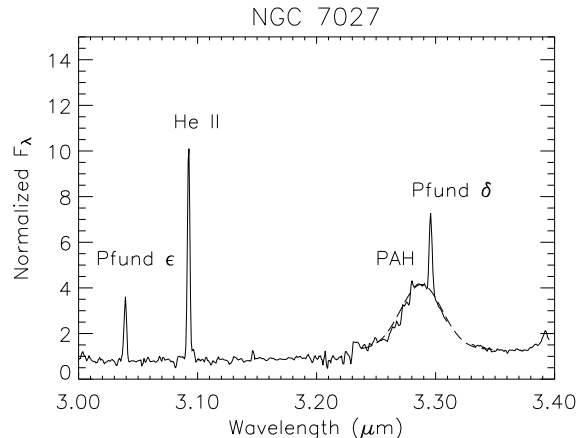


FIG. 1.— Spectrum of NGC 7027 with prominent emission features labelled. The missing data from 3.31 to 3.33 μm is not plotted due to saturated atmospheric methane and water features. The dashed line shows the gaussian fit to the data.

correction steps described above removes the majority of these features, even the best spectrum, that of NGC 7027, shows residual structure. It should be noted that these complications exist, although to a much reduced level, even at the world's best astronomical sites, such as Mauna Kea. However, with the caveat on the limitations of the telluric corrections, we can analyze the detected PAH emission features. Figure 1 shows the extracted 3.3 μm spectrum for NGC 7027. Of course, NGC 7027 is a particularly bright, high-excitation planetary nebula with well-known PAH emission in all bands. Hydrogen and helium lines are seen in emission, as is the broad PAH feature. One hydrogen line, Pfund delta (3.296 μm) is seen in emission on top of the broad PAH feature. Also evident is the effect of residual terrestrial water absorption. The blue slope of the PAH feature has several unsaturated, but variable water absorption features, leading to a slightly stair-stepped shape even on NGC 7027. On the red slope, there is a deep atmospheric methane line at 3.32 μm . This line cannot be removed from the spectrum, thus no data points are plotted for the 3.310-3.330 μm region.

The FLITECAM spectra presented here cover from 3.0 to 3.4 μm at a resolution of $R \sim 1700$. After reduction, all spectra underwent a 5-sigma cut to remove hot pixels and residuals from saturated atmospheric lines. Figures 2 and 3 show a selection of the target spectra all plotted in a similar way. There are four classes of resulting spectra: 1) continuum objects, 2) PAH non-detections, 3) PAH detections and 4) PAH possible detections. (See Table 1 again for a list of all observed PNs and their classification.)

4.2. Continuum objects

Four members of the sample exhibit a stellar spectrum with no obvious emission features. All four of these objects are post-AGB or AGB stars, and are thus less evolved than the rest of the sample. RAFGL 3116 does have reported PAH detections at longer wavelengths from ISO observations (Jourdain de Muizon et al. 1990), but does not show an obvious PAH 3.3 μm band peak in our observations. The feature may be present, but could

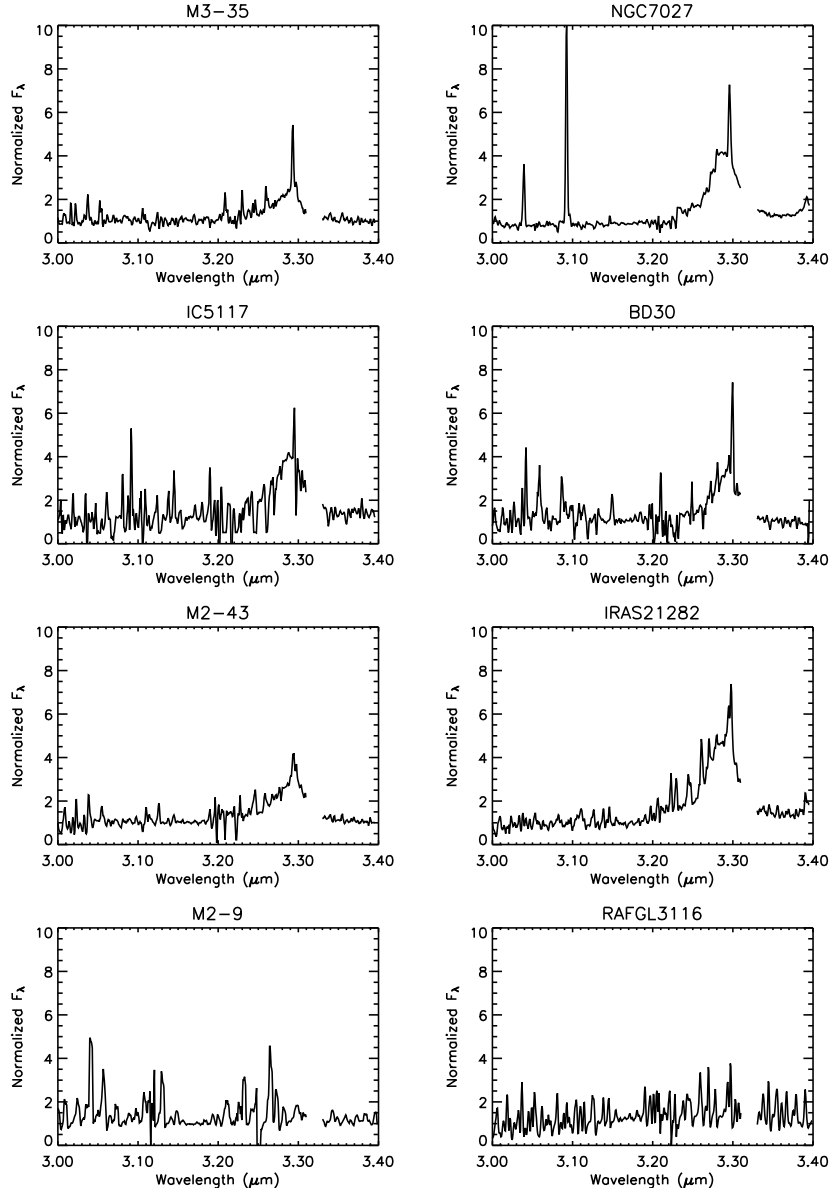


FIG. 2.— Reduced spectra from PAH survey. The missing data from 3.31 to 3.33 μm is not plotted due to saturated atmospheric methane and water features. Fainter objects show noise spikes in the 3.0 to 3.2 μm region due to terrestrial absorption lines. Detected emission lines are listed in Table 2. All detected PAH features are well-fitted by a Gaussian curve. IRAS 21282 shows some non-symmetry, but has FWHM and peak PAH wavelength emission consistent with class A_{3.3} emission.

be swamped by the strong, red spectrum of the highly evolved AGB star. The spectrum of RAFGL 3116 in Figure 2 is typical of this type of object.

4.3. PAH non-detections

Three members of the sample (M 2-9, NGC 3234, and NGC 6210) exhibit standard PN features (i.e. atomic emission lines and non-existent or very faint continuum), but yet show no PAH emission at 3.3 μm . All three non-detections have an oxygen-rich chemistry, with $\text{C}/\text{O} < 1$. In these objects, crystalline silicate features tend to dominate, rather than PAH emission (Allamandola 1989). M 2-9 in Figure 2 is an example of a oxygen-rich planetary nebula with no PAH emission.

4.4. PAH detections and possible detections

Eleven members of the sample show distinct PAH emission at 3.3 μm , while two more targets (WHME-1 and J900) show possible PAH emission. PAH flux was quantified by fitting a gaussian to the PAH band assuming a flat continuum. NGC 7027 is the best example of a strong PAH detection, and can be seen either in Figure 1 or Figure 2. WHME-1 and J900 are examples of possible-detection of PAH emission. While PAH emission is seen at longer wavelengths in these objects, the nebulae may have been too faint compared to the high backgrounds at Lick for solid 3.3 μm detections. Figures 2 and 3 show the extracted spectra for all the PAH detections. Hydrogen emission at 3.296 μm is evident in many of the sources with a PAH detection (HB 5, M3-35, BD+30°3639 and NGC 7027 in particular). This profile was subtracted out of the extracted spectra by fitting a

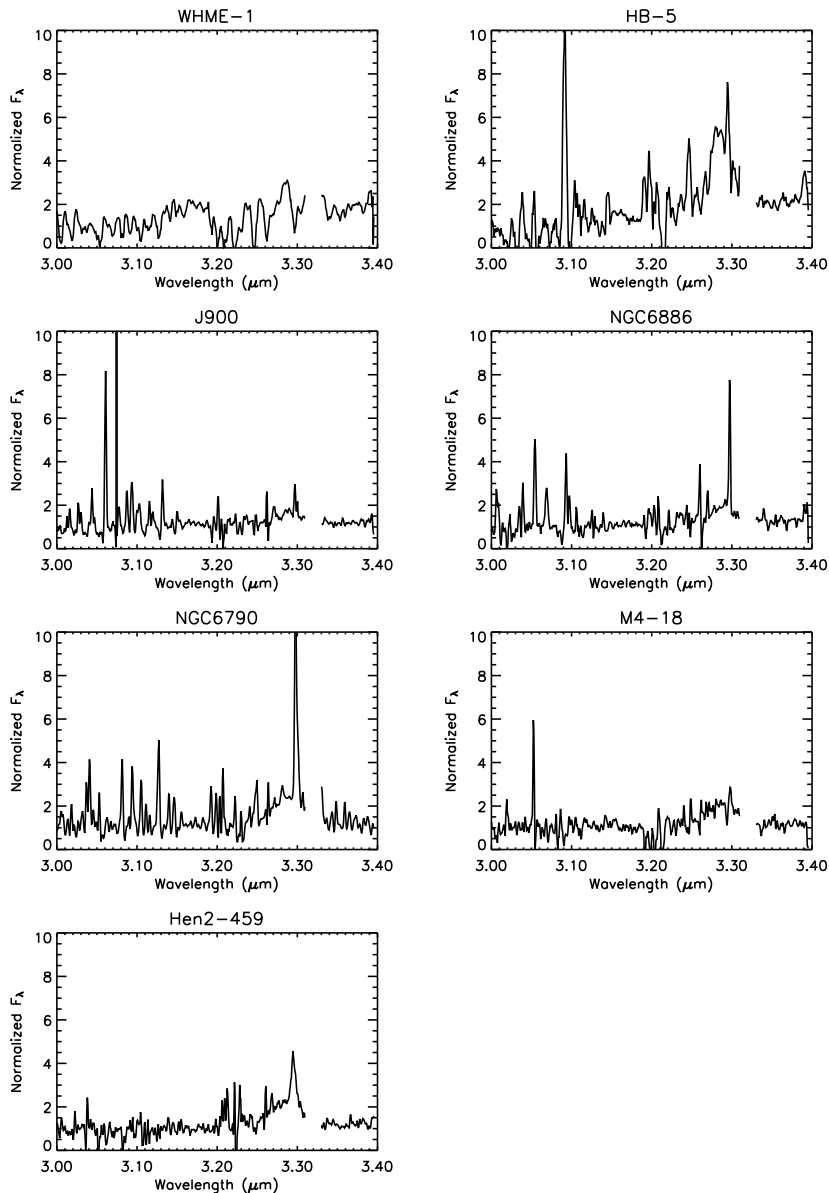


FIG. 3.— Reduced spectra from PAH survey. The missing data from 3.31 to 3.33 μm is not plotted due to saturated atmospheric methane and water features. Fainter objects show noise spikes in the 3.0 to 3.2 μm region due to terrestrial absorption lines. Detected emission lines are listed in Table 2. All detected PAH features are well-fitted by a Gaussian curve.

gaussian before fitting a curve to the PAH band itself in order to determine its strength and shape. Table 2 summarizes the derived PAH measurements for the observed nebulae. Those nebulae with non detections have upper limits on the PAH equivalent widths. The C/O ratios of the nebulae, if known, are also listed.

5. DISCUSSION AND ANALYSIS

Prior to further analysis, each detected PAH feature was fitted with a gaussian to determine the feature's FWHM and central wavelength. The average central wavelength of the PAH emission feature was $3.288\mu\text{m} \pm 0.002\mu\text{m}$, with a FWHM of $0.042\mu\text{m} \pm 0.002\mu\text{m}$. This is consistent with surveys of similar objects that show this feature to have a gaussian profile centered at $3.289\mu\text{m}$ and a FWHM of $0.042\mu\text{m}$ (Tokunaga et al. 1991).

For more detailed analysis of the $3.3\mu\text{m}$ feature we

adopt the method used by Roche et al. (1996), that is, we quantify PAH emission strength by determination of the emission band's equivalent width (EW). This method is superior to absolute flux measurements as the EW is less affected by atmospheric absorption and fluctuation. However, the determination of equivalent width depends on an accurate model of continuum emission for comparison to the measured feature, and can thus be rendered inaccurate for objects with weak continua, or in regions where emission plateaus mask true continuum emission. As this survey was limited in scope to only the brightest, most compact planetary nebula, most of the observed objects exhibited continuum emission above the threshold necessary for good equivalent width determination. The wavelength regime of this study ($3.0\text{--}3.4\mu\text{m}$) is also advantageous to determining continuum emission levels, because the region just blue of the PAH emission is rela-

TABLE 2
TARGET PROPERTIES AND PAH RESULTS

Object	Class	C/O ^(a) Ratio	PAH EW (nm)	PAH FWHM (μ m)	Cent. Wave. (μ m)	Other Lines ^(d) ID (EW(nm))
M 3–35	A _{3.3}	—	67.3 \pm 4.9	0.041 \pm 0.004	3.287 \pm 0.002	3(11)
NGC 7027	A _{3.3}	2.15	170.6 \pm 5.7	0.041 \pm 0.002	3.289 \pm 0.002	1:(12); 2:(51); 3(32)
HB 5	A _{3.3}	—	80.3 \pm 4.5	0.042 \pm 0.002	3.285 \pm 0.003	2:(31); 3(9)
IC 5117	A _{3.3}	1.92	113.3 \pm 7.5	0.038 \pm 0.005	3.289 \pm 0.002	3(16)
BD+30°3639	A _{3.3}	1.6	78.6 \pm 8.4	0.040 \pm 0.003	3.289 \pm 0.003	3(11)
M 2–43	A _{3.3}	—	66.7 \pm 4.9	0.045 \pm 0.004	3.289 \pm 0.002	3(11)
IRAS21282	A _{3.3}	—	166.1 \pm 9.8	0.042 \pm 0.004	3.286 \pm 0.002	3(15)
Hen 2-459	A _{3.3} ^(b)	—	46.6 \pm 5.2	0.041 \pm 0.004	3.287 \pm 0.002	3(26)
WHME-1	A _{3.3} ^(b)	—	14.9 \pm 9.3 ^(b)	0.062 \pm 0.010	3.286 \pm 0.035	
J900	A _{3.3}	4.39	14.4 \pm 7.1 ^(b)	0.041 \pm 0.004	3.289 \pm 0.002	3(<5.6)
NGC 6886	A _{3.3}	1.3	46.2 \pm 10.8	0.043 \pm 0.004	3.290 \pm 0.003	3(27)
NGC 6790	A _{3.3}	0.82	57.4 \pm 11.4	0.041 \pm 0.003	3.289 \pm 0.002	3(37)
M 4-18	A _{3.3}	2.9	60.0 \pm 33.4 ^(c)	0.047 \pm 0.003	3.286 \pm 0.002	
AFGL 3068	ND	—	<6.2	—	—	
AFGL 3116	ND	—	<7.7	—	—	
AFGL 337	ND	—	<7.6	—	—	
YY Tri	ND	—	<6.2	—	—	
M 2-9	ND	<0.5	<9.2	—	—	
NGC 3242	ND	0.67	<4.3	—	—	
NGC 6210	ND	0.26	<9.1	—	—	

^a C/O ratio references; NGC 7027: Middlemass (1990); IC 5117, NGC 3242: Kholtygin (1998); NGC 6886: Pwa et al. (1986); NGC 6790, NGC 6210: Liu et al. (2004); M 4-18: De Marco & Barlow (2001); M 2-9: Liu et al. (2001)

^b Borderline PAH detection

^c Noisy Continuum

^d 1: Pfund ϵ (3.039 μ m), 2: HeII(3.09 μ m), 3: Pfund δ (3.29 μ m). EW is listed with Line ID.

tively free of atmospheric absorption bands, and is constant over a range roughly comparable to the width of the PAH feature. Three nebulae have unusable equivalent width measurements due to either weak PAH emission (as in WHME1 and J900), or noisy continuum spectra (as in M 4-18).

5.1. Correlating PAH and C/O ratio

The most well-studied correlation is between the nebular C/O ratio and the PAH emission strength. Current theory predicts that nebulae with high C/O ratios will exhibit PAH emission, while more oxygen rich nebulae will exhibit silicate features, having trapped most nebular C/O in CO molecules. Figure 4 shows the derived 3.3 μ m emission equivalent width plotted against the nebular C/O ratio obtained from the literature (Kholtygin 1998). Only 7 nebulae in our sample have known C/O ratios, and only 5 of these nebulae have usable equivalent widths. PAH emission equivalent widths are uncertain up to 10 percent, and even the known C/O ratios measurements have large uncertainties.

Figure 4 shows the C/O ratio plotted against the five nebulae with measured equivalent widths. Also plotted is the linear regression fit to the data. This shows a PAH equivalent width detection threshold at C/O=0.65 \pm 0.28. This result is within the uncertainties obtained by Roche et. al. (1996), who performed a similar analysis, and with Cohen & Barlow (2005), who measured a C/O ratio versus 7.7 μ m PAH emission.

5.2. PAH emission classification

For further analysis we characterize the PAH emission according to the system suggested by van Dierendonck et al. using band shape, location and FWHM. Class

A_{3.3} emission is characterized by symmetric PAH emission centered at 3.290 μ m with a FWHM of 0.040 μ m. Class B_{3.3} emission is centered at 3.293 or 3.297 μ m with a FWHM of 0.030 μ m. In van Dierendonck's survey planetary nebulae were classified as class A sources. Tokunaga et al. (1991) used similar criteria to categorize 3.3 μ m emission, with their class 1 equivalent to the van Dierendonck's class A_{3.3}. The results of this classification are listed in Table 2. All sources with PAH emission are of class A_{3.3}, as is consistent with both van Dierendonck and Tokunaga. The presence of strong atmospheric water lines makes analysis of PAH emission line shape more difficult, but all detected PAH features have FWHM and central emission wavelengths consistent with class A_{3.3} emission, and appear to be largely symmetric. Other surveys of 3.3 μ m emission in planetary nebulae (Roche et al. 1996) were at lower resolution than the R=1700 spectra in this study. Our resolution allows us to fit and remove the Pfund delta hydrogen emission line, which could otherwise affect the fitted gaussian curve and apparent line shape.

The 3.3 μ m feature shows relatively little variation even in very different emission sources (van Dierendonck 2004, Cohen & Barlow 2005, Tokunaga 1991), while longer wavelength PAH emission shows greater variation in central wavelength and FWHM (Peeters et al. 2002). In longer wavelength studies planetary nebulae are classified as class B_{6–9} objects, while some very young post-AGB stars exhibit class C_{6–9} emission. This apparent evolution in PAH emission during the AGB to planetary nebula transition is the primary motivation for expanding the sample of evolved stars investigated at high resolution in all PAH bands.

In the current survey we did not sample multiple por-

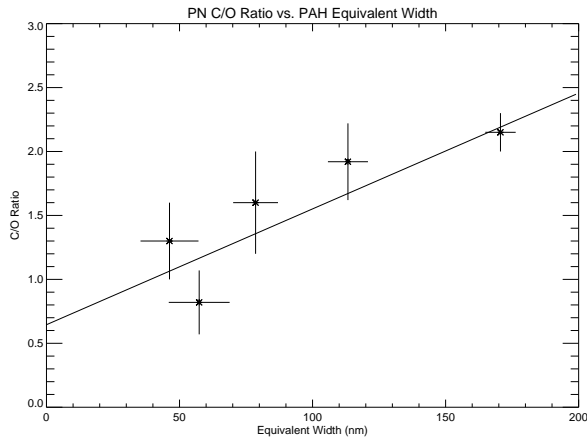


FIG. 4.— PN C/O Ratio versus measured PAH EW. See Table 2 for data and references. The plotted line yields a threshold value of $C/O=0.65 \pm 0.28$

tions of the target objects, instead sampling a 4-5 arcsec band across the extent of the nebula. If there are more subtle changes in $3.3 \mu\text{m}$ emission due to nebular position, they would not be detected by this approach.

6. CONCLUSIONS

With a resolution $\sim 1,700$ we have carried out a preliminary survey of $3.3 \mu\text{m}$ PAH emission using FLITECAM, an instrument developed at UCLA, on the Lick Observatory 3-m telescope. This survey is a pilot project for a deeper program to be carried out using the same instrument on board the Stratospheric Observatory for Infrared Astronomy (SOFIA).

(1) Out of 20 objects observed, 11 showed detectable $3.3 \mu\text{m}$ PAH emission.

(2) We found the $3.3 \mu\text{m}$ feature to have a FWHM and central wavelength consistent with that found by Tokunaga et al. (1991), Roche et al. (1996) and van Diedenhoven et al. (2004).

(3) A correlation was found between C/O ratio and PAH emission strength, consistent with that reported by

Roche et al. (1996) and Cohen & Barlow (2005). We calculate a threshold C/O ratio of 0.65 ± 0.28 .

(4) We classified the 11 objects showing PAH emission according to the system suggested by van Diedenhoven.

Our high-resolution survey of $3.3 \mu\text{m}$ emission has expanded the sample of PNs with characterized PAH emission at this wavelength. This step is important for evolutionary studies because shifts are seen in longer wavelength PAH emission between PNs and their evolutionary pre-cursors. It also serves as a starting point for detailed studies of spatial variations of PAH emission in individual planetary nebulae, as well as studies of PAH emission in young AGB stars.

Although the sample of objects presented is relatively small, these high-resolution $3.3 \mu\text{m}$ PAH spectra provide a clear indication of the importance of airborne astronomy to this field. With SOFIA, the thermal background will be reduced by more than an order of magnitude and none of the water vapor lines will saturate. Higher signal-to-noise ratios will be possible, and it may soon be practical to detect subtle changes in line shape due to PAH ionization. Studies of the $3.3 \mu\text{m}$ band in Orion have shown a shift from class A_{3.3} to class B_{3.3} emission with position (van Diedenhoven et al. 2004), as well as a shift from symmetric to asymmetric $3.3 \mu\text{m}$ emission. Similar shifts may occur in planetary nebulae, and would be observable with lower backgrounds and water vapor contributions. Likewise, in extended objects the lower backgrounds will make it possible to probe the shape of the PAH feature across the spatial extent of the nebula.

The authors wish to thank the staff of the Lick Observatory for their outstanding support. We also thank Eric Becklin (UCLA) for his support throughout the development of the FLITECAM instrument. E.C.S. is supported by a NASA Graduate Student Research Program (GSRP) fellowship. The authors wish to thank the anonymous referee, Dr. Mike Jura and Dr. Mark Morris for their helpful suggestions in improving this manuscript.

REFERENCES

- Allamandola, L. J., Tielens, G. G. M., & Barker, J. R. 1989, *ApJS*, 71, 733
- Cohen, M., & Barlow, M. J. 2005, *MNRAS*, 362, 1199
- Cohen, M., Tielens, A. G. G. M., Bregman, J., Witteborn, F. C., Rank, D. M., Allamandola, L. J., Wooden, D., & Jourdain de Muizon, M. 1989, *ApJ*, 341, 246
- De Marco, O., & Barlow, M. J. 2001, *Ap&SS*, 275, 53
- Geballe, T. R., Lacy, J. H., Persson, S. E., McGregor, P. J., & Soifer, B. T. 1985, *ApJ*, 292, 500
- Gillett, F. C., Forrest, W. J., Merrill, K. M., Soifer, B. T., & Capps, R. W. 1975, *ApJ*, 200, 609
- Gillett, F. C., Forrest, W. J., & Merrill, K. M. 1973, *ApJ*, 183, 87
- Hony, S. 2002, Ph.D. Thesis
- Jourdain de Muizon, M., Cox, P., & Lequeux, J. 1990, *A&AS*, 83, 337
- Justtanont, K., Skinner, C. J., Tielens, A. G. G. M., Meixner, M., & Baas, F. 1996, *ApJ*, 456, 33
- Kholtygin, A. F. 1998, *A&A*, 329, 691
- Leger, A., & Puget, J. L. 1984, *A&A*, 137, L5
- Liu, Y., Liu, X.-W., Barlow, M. J., & Luo, S.-G. 2004, *MNRAS*, 353, 1251
- Liu, X.-W., et al. 2001, *MNRAS*, 323, 343
- Lord, S. D. 1992, NASA TM103957
- Mainzer, A. K., & McLean, I. S. 2003, *ApJ*, 597, 555
- Mainzer, A. K., McLean, I. S., Sievers, J. L., & Young, E. T. 2004, *ApJ*, 604, 832
- Matsuura, M., et al. 2005, *A&A*, 434, 691
- McLean, I. S., Smith, E. C., Aliado, T., Brims, G., Kress, E., Magnone, K., Milburn, J., Oldag, A., Silvers, T., & Skulason, G. 2006, *Proc. SPIE*, 6269.
- Middlemass, D. 1990, *MNRAS*, 244, 294
- Peeters, E., Hony, S., Van Kerckhoven, C., Tielens, A. G. G. M., Allamandola, L. J., Hudgins, D. M., & Bauschlicher, C. W. 2002, *A&A*, 390, 1089
- Pwa, T. H., Pottasch, S. R., & Mo, J. E. 1986, *A&A*, 164, 184
- Rinehart, S. A., Houck, J. R., Smith, J. D., & Wilson, J. C. 2002, *MNRAS*, 336, 66
- Roche, P. F., Lucas, P. W., Hoare, M. G., Aitken, D. K., & Smith, C. H. 1996, *MNRAS*, 280, 924
- Sellgren, K. 1984, *ApJ*, 277, 623
- Sloan, G. C., et al. 2007, *ApJ*, 664, 1144
- Smith, E. C., & McLean, I. S. 2006, *Proc. SPIE*, 6269, 50
- Tokunaga, A. T., Sellgren, K., Smith, R. G., Nagata, T., Sakata, A., & Nakada, Y. 1991, *ApJ*, 380, 452
- van Diedenhoven, B., Peeters, E., Van Kerckhoven, C., Hony, S., Hudgins, D. M., Allamandola, L. J., & Tielens, A. G. G. M. 2004, *ApJ*, 611, 928